Rapidly fabricated carbon/carbon composites with a mesophase pitch binder and graphite flake filler with excellent EMI shielding and thermal conductivity

Luo Pengfei, Tian Shan, Guo Fengjun, Xiao Zhichao*

(*State Key Laboratory for Mechanical Behavior of Materials, School of Materials Science and Engineering, Xi'an Jiaotong University, Xi'an* 710049, *China*)

Abstract: Carbon/carbon (C/C) composites are ideal materials for electromagnetic interference (EMI) shielding and thermal management in the aerospace field because of their low density. However, traditional C/C composites primarily rely on repeated densification to increase their EMI shielding effectiveness (*SE*), which not only increases density but also involves lengthy preparation cycles. We have constructed a unidirectional (1D) C/C composite using a matrix of mesophase pitch-derived carbon and graphite flakes, reinforced with mesophase pitch-based carbon fibers. Using a one-step consolidation process produced by spontaneous assembly during heating, the open pores and a continuous conductive network give the composite an EMI *SE* of up to 83.97 dB in the 8.2–12.4 GHz (X-band). The material also has a thermal conductivity of 191.84 $W \cdot m^{-1} \cdot K^{-1}$ and an electrical conductivity of 6.50×10^4 $S \cdot m^{-1}$ along the fiber direction, together with a flexural strength exceeding 100 MPa, while having a bulk density of only 1.01 $g \cdot cm^{-3}$. This work therefore presents a short-cycle fabrication strategy for low-density C/C composites that integrate high EMI *SE*, efficient thermal management, and good mechanical properties.

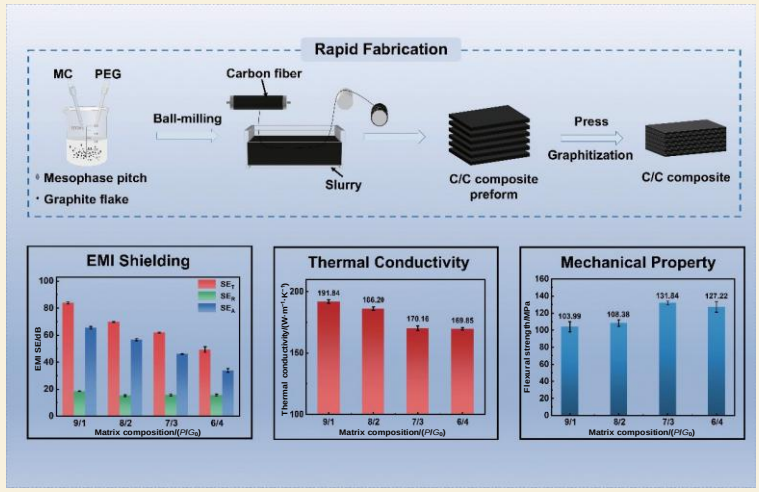

Key words: Carbon/carbon (C/C) composites; Mesophase pitch; Electromagnetic interference (EMI) shielding; Thermal conductivity; Electrical conductivity

1 Introduction

The rapid advancement of emerging technologies, including fifth-generation (5G) mobile communications, artificial intelligence (AI), the Internet of Things (IoT), and new energy vehicles, is propelling an evolution in electronic devices toward higher power density, greater integration, and miniaturization[1–2]. This trend, however, results in significant heat accumulation and continuously rising thermal flux density during the operation of devices, while electromagnetic interference (EMI) has also become increasingly severe[3–6]. Traditional single-function materials, which often provide only limited shielding capabilities, fail to meet these stringent multifunctional requirements. Therefore, creating structurally integrated composites that simultaneously offer excellent EMI shielding effectiveness (*SE*), efficient thermal management, and mechanical reliability has become a vital research goal, key to advancing next-generation electronics.

Owing to their lightweight nature, excellent corrosion resistance, and ability to withstand high temperatures, carbon-based materials stand out among

Received: November 17, 2025
Revised: February 07, 2026
Accepted: February 12, 2026

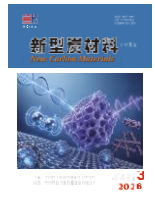

mainstream EMI shielding options such as metals and conductive polymers. This makes them particularly suitable for weight-sensitive applications including satellites, aerospace vehicles, and automobiles, where their low density offers a distinct advantage. However, conventional carbon materials (e.g., carbon foams[7] and aerogels[8]) often suffer from poor mechanical properties, limiting their application as structural components. To address this issue, carbon/carbon (C/C) composites reinforced with high-strength carbon fibers have gained prominence. These composites exhibit exceptional properties, including high-temperature resistance, high specific strength, and high specific modulus[9–11]. Notably, after high-temperature graphitization, C/C composites exhibit metal-like thermal and electronic conductivity[12–14]. Conventional fabrication processes for C/C composites, including multi-cycle chemical vapor infiltration (CVI)[15], polymer infiltration and pyrolysis (PIP)[16], and high-temperature hot pressing[17], achieve EMI shielding primarily through surface reflection. This mechanism depends critically on forming continuous conductive networks on the material surface, which requires substantial increases in bulk density. For instance, Xue et al. reported an exceptional EMI *SE* of ~80 dB in the X-band for C/C composites, achieved at a bulk density of 1.85 g·cm^{-3} by repeated CVI and PIP densification followed by 3000 °C graphitization[18]. However, this reliance on high-density construction fundamentally conflicts with the essential requirements for lightweight advanced materials. Furthermore, these conventional techniques are inherently plagued by prolonged processing cycles and substantial energy consumption. These drawbacks severely restrict their use in cost-sensitive, high-volume applications, creating a significant bottleneck for meeting the rapid innovation demands of the modern electronics industry[19–20].

Research has shown that porous structures significantly enhance EMI *SE* through improved impedance matching, which boosts the shielding effectiveness of absorption, and extensive internal scattering that promotes wave attenuation[21–23]. Building on this principle, this study employed mesophase pitch as the binder in C/C composites, primarily owing to its excellent fluidity during thermal processing and its capacity to form a porous carbon structure after carbonization[24]. Compared to most of resin polymers, mesophase pitch offers higher carbon yield and superior graphitization potential[25]. However, during the carbonization process, the volatilization of components within the pitch can cause expansion, resulting in undesirable density reduction and degradation of mechanical property[26]. Incorporating fillers such as carbon black, needle coke, and graphite flakes can promote cross-linking of the pitch and effectively suppress this expansion[17,27–28]. Among these options, graphite flakes were selected as the optimal filler in this work due to their exceptionally high in-plane thermal and electronic conductivity[29]. Furthermore, mesophase pitch-based carbon fibers act as the reinforcement, forming continuous thermally and electrically conductive networks while providing robust structural support throughout the composite. During heat treatment, a stable porous structure spontaneously forms through the combined supporting roles of the carbon fibers and graphite flakes, along with the binding action of pitch. This synergy effect successfully consolidates the traditional multi-step densification into a single-step process.

Our study demonstrates that the mesophase pitch to graphite flake weight ratio (P:G) in the carbon matrix precursor plays a critical role in determining the microstructural characteristics and properties of the composites. When the P∶G ratio is 9∶1, the fabricated C/C composite maintains a low density of 1.01 g·cm^{-3} while displaying exceptional integrated performance, including an X-band EMI *SE* of 83.97 dB, a thermal conductivity of 191.84 W·m^{-1}·K^{-1} and an electronic conductivity of 6.50×10^4 S·m^{-1} in the *X*-direction, along with a flexural strength of 103.99 MPa. This research establishes an innovative approach for rapid fabrication of low-density, high-performance C/C composites and highlights their promising potential as multifunctional EMI shielding materials in satellites, aerospace vehicles, and auto-

mobiles engineering applications.

2 Experimental

2.1 Material preparation

The fabrication process of the C/C composites is illustrated in Fig. 1. Initially, mesophase pitch powder (granule of diameter < 75 μm, with a softening point of about 300 °C and carbon yield of about 70%, supplied by Shaanxi Tiance New Material Technology Co. Ltd., Shaanxi, China) and graphite flakes (granule of diameter < 48 μm, high purified flake 99%, supplied by Zhudun Metal Materials Co. Ltd., Hebei, China) were mixed at a specified mass ratio. Anhydrous ethanol was added as the solvent at a 1∶1 weight ratio (solvent to solids), followed by the dropwise addition of a 10% methylcellulose (MC) aqueous solution (as thickening agent) and a 5% polyethylene glycol (PEG) solution (as dispersing agent). A homogeneous slurry was subsequently obtained by wet ball milling the mixture for 8 h. The slurry was uniformly coated onto mesophase pitch-based carbon fibers (TC-20, supplied by Shaanxi Tiance New Material Technology Co.) to produce a 1D carbon fabric, which was then dried. The dried fabric was cut and stacked into a preform. This preform was then carbonized at 1000 °C with a holding time of 2 h, followed by graphitization at 3150 °C for 40 min, to yield the final C/C composites. The C/C composites matrices, prepared with mesophase pitch powder to graphite flake weight ratios of 9∶1, 8∶2, 7∶3, and 6∶4, are designated as C/C-1, C/C-2, C/C-3, and C/C-4, respectively. The carbon fiber volume fraction for all composites is determined to be approximately 20% based on calculation.

2.2 Characterization

The porosity and bulk density were determined using the Archimedes method with the water impregnation. The open porosity P_{open} of the samples is calculated using Eq. (1):

$$P_{open} = \frac{m_2 - m_3}{m_2 - m_1} \quad (1)$$

where m_1 is the saturated sample weight when submerged in water, m_2 is the saturated weight (assumed that all pores are filled with water), and m_3 is the dry weight of the sample. With reference to the density of water (ρ_0), the sample density (ρ) was calculated according to Eq. (2):

$$\rho = \rho_0 \frac{m_3}{m_2 - m_1} \quad (2)$$

The microstructure of the C/C composites was characterized using scanning electron microscopy (SEM, FEI VERIOS 460). Phase composition was analyzed by X-ray diffraction (XRD, Bruker D8 ADVANCE). Raman spectroscopy was performed using a Raman spectrometer with a 532 nm excitation laser, sampling the pitch carbon surrounding the carbon fibers within the *XY* plane. Electrical conductivity was determined by a four-point probe method (FT-340,

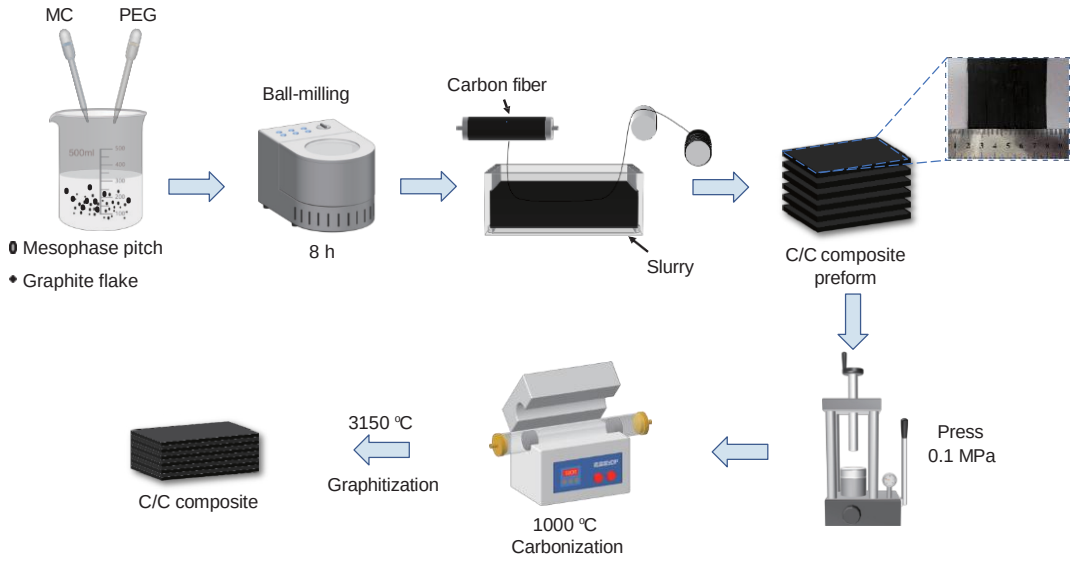

Fig. 1 The fabrication procedure and photographs of C/C composites

Rooko Intelligent Technology, China). Mechanical properties were evaluated on a UTM6103 universal testing machine at a loading rate of 0.5 mm·min^{-1} using specimens sized 3 mm × 4 mm × 36 mm. Thermal conductivity was measured at room temperature via the laser flash method (LFA 447, NETZSCH, Germany). Temperature distribution was monitored and recorded using an infrared camera (Fotric 250, Beijing, China). EMI *SE* was characterized with a vector network analyzer (N5244B, Keysight, USA), with the C/C composites samples cut into dimensions of 22.84 mm × 10.13 mm × 2 mm for the measurement.

3 Results and discussion

3.1 Microstructures of C/C composites

Fig. 2(a-d) display optical images of carbon matrices prepared with different P∶G ratios. At 9∶1, the matrix shows a loose structure due to the expansion of mesophase pitch during carbonization caused by its volatility, which generates extensive pores and cracks. As illustrated in Fig. 2(b-d), increasing the graphite flake proportion effectively suppresses pitch expansion, improves carbon yield, and fills voids[30−31], leading to compact matrix structures at P∶G ratios of 7∶3 and 6∶4.

Fig. 2(e-h) further demonstrates the governing role of graphite flake proportion in the matrix densification. With increasing flake content, the structure progressively transforms from an initially porous morphology to a densely consolidated state. The bulk density and open porosity of the carbon matrices are shown in Table S1. As the P∶G ratio decreases, the bulk density gradually increases while the open porosity gradually decreases. As observed in Fig. 2(g-h), when the P∶G ratios were 7∶3 and 6∶4, the increased graphite flake content promoted pitch crosslinking, significantly reducing open porosity and microcracks. Under these conditions, mesophase pitch acts as an efficient binder, integrating the graphite flakes into a coherent monolith with a well-developed dense microstructure.

Fig. 3(b-i) displays the microstructure of the C/C composites, revealing pronounced structural anisotropy. In the *XY* plane of C/C-1, the carbon fibers are highly ordered, with a highly oriented pitch carbon layer forming around them. This ordered structure results from the templating effect of the aligned carbon fibers, which guide the planar macromolecules of mesophase pitch to orient parallel to the fiber axis, thereby establishing a long-range ordered architecture, the resulting ordered carbon layer significantly enhances both the thermal and electrical conductivity of the composites[32]. However, as observed in Fig. 3(c-e), the fiber distribution becomes progressively more disordered. This trend occurs because the reduced mesophase pitch binder proportion weakens the bonding between fiber bundles, impeding their collective alignment into a uniform orientation. Concurrently, the distribution of ordered pitch carbon layers around the fibers becomes disordered, forming randomly oriented domains that disrupt the long-range structural order.

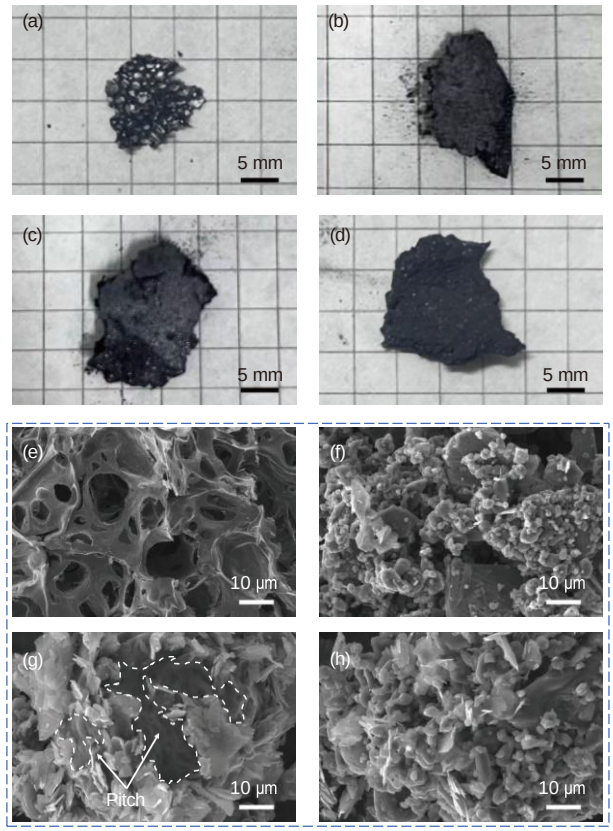

Fig. 2 (a-d) Optical images and (e-h) SEM images of the carbon matrix with different P∶G ratios. (a, e) 9∶1, (b, f) 8∶2, (c, g) 7∶3, and (d, h) 6∶4

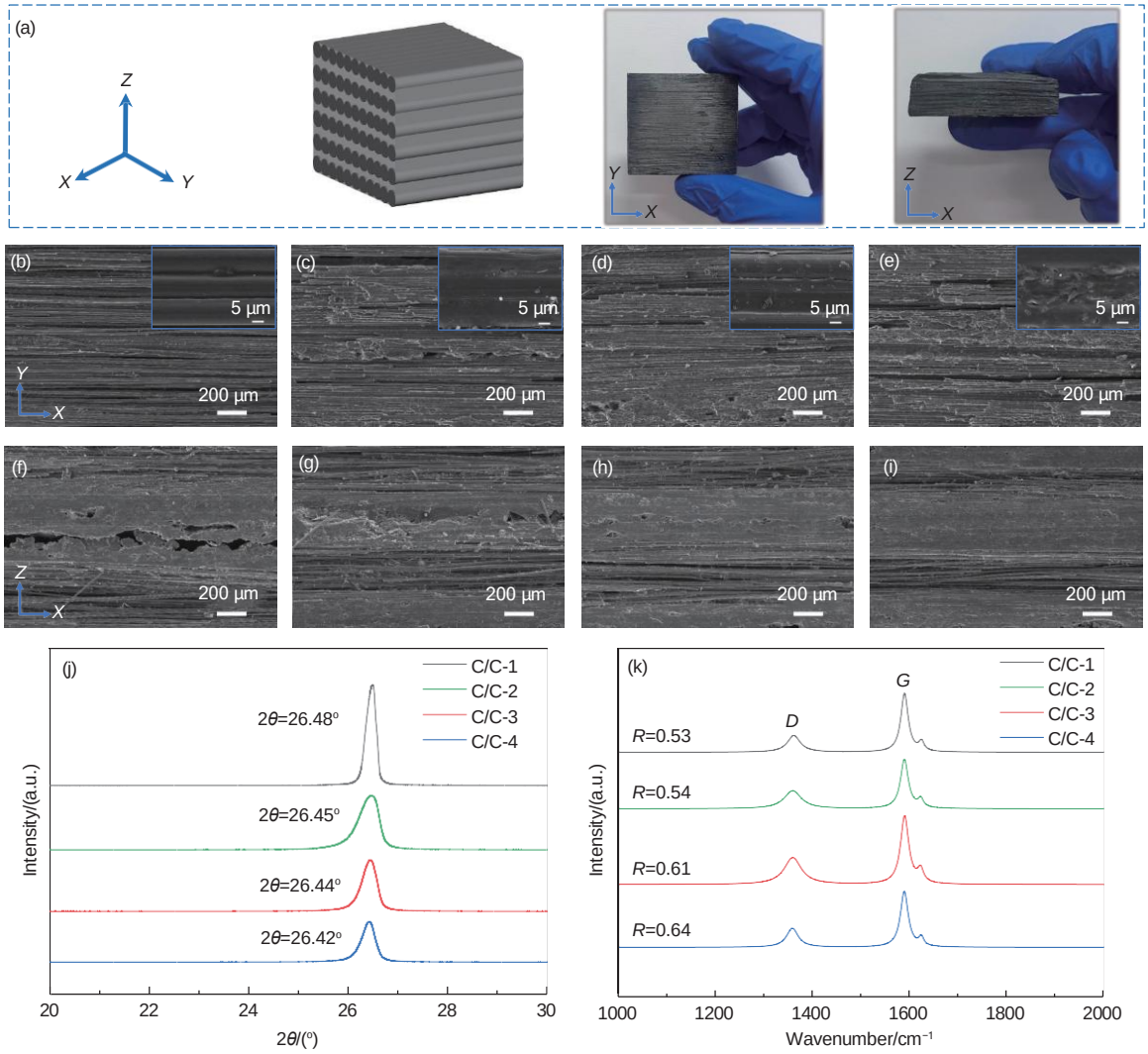

Fig. 3 (a) Schematic of C/C composites orientation and optical images. (b-i) SEM images on the (b-e) *XY*- and (f-i) *XZ*-planes of the C/C composites: (b, f) C/C-1, (c, g) C/C-2, (d, h) C/C-3, (e, i) C/C-4. (j) XRD patterns and (k) Raman spectra of the C/C composites

As shown in Fig. 3(f-i), the interlaminar transition zone in the *XZ* plane is composed of pitch carbon and graphite flakes. In C/C-1, this region exhibits numerous cracks and voids. As the graphite proportion increases, these defects are significantly reduced because the voids and cracks left by the pyrolytic volatilization of the pitch are effectively filled[30]. This leads to a substantial improvement in the degree of densification along the *Z* direction.

As shown in Fig. 3j, the XRD patterns of all 4 C/C composites exhibit strong diffraction peak at 26.5°, which is attributed to the interplanar spacing d_{002} of graphite, indicating that the composites formed a well-developed graphitized structure after graphitization[33]. The graphitization degrees (g) of the C/C composites were calculated according to the Eq. (3)[34]:

$$g = \frac{d_{002} - 0.3440}{0.3354 - 0.3440} \tag{3}$$

where 0.3354 (nm) is the interlayer spacing of ideal graphite crystals, 0.3340 (nm) corresponds to that of fully amorphous carbon, and d_{002} denotes the measured average interlayer spacing of the (002) plane. The value of d_{002} was obtained from X-ray diffraction (XRD) patterns using Bragg's law[34]:

$$d_{002} = \frac{\lambda}{2\sin\theta} \tag{4}$$

where λ is the X-ray wavelength and θ is the diffraction angle of the (002) peak. Calculations indicated graphitization degrees of 85.6%, 81.7%, 80.2% and 78.5% for C/C-1, C/C-2, C/C-3 and C/C-4, respect-

ively. The highest value for C/C-1 corresponds to its largest grain size, smallest interlayer spacing, and most ordered crystal plane arrangement. With a decreasing P∶G ratio in the matrix, the grain size is reduced and the interlayer spacing gradually increases, leading to a corresponding decline in the graphitization degree. The dominant factor here is the steric hindrance imposed by the graphite flakes, which disrupts the ordered alignment of the surrounding mesophase pitch molecules during heat treatment. This restriction inhibits the complete polymerization and orientation of the pitch molecules, consequently suppressing the growth and perfection of graphite crystals[35–37].

The Raman spectra (Fig. 3k) show 2 characteristic peaks near 1360 and 1580 cm^{-1} for all samples, corresponding to the *D* band of disordered carbon structures and the *G* band of graphitic lattice structures, respectively. The *G* band is generally regarded as an intrinsic characteristic peak of natural graphite. The intensity ratio of I_D/I_G (denoted as the *R* value) is commonly used to evaluate the graphitization degree of the materials, where a lower *R* value indicates a higher graphitization degree[38]. Fig. 3k shows a gradual increase in the *R* value as the proportion of graphite flakes in the matrix rises, indicating a decreasing in the graphitization. The Raman spectroscopy results, combined with XRD analysis and the progressively disordered arrangement of pitch carbon around the fibers observed in the *XY* plane (Fig. 3(b–e)), collectively confirm that a higher graphite flake content impedes the ordered alignment of the carbon matrix during graphitization, leading to a lower graphitization degree.

The bulk density and open porosity of the C/C composites with different matrix ratios are summarized in Table S2. All composites exhibited bulk densities below 1.10 $g·cm^{-3}$. A decrease in the P∶G ratio of the matrix leads to an increase in bulk density and a concurrent decrease in open porosity from 33.02% to 24.55%. This trend was attributed to the increased proportion of graphite flake filler, which effectively inhibited matrix expansion and filled voids and cracks, thereby preserving the structural integrity[39].

3.2 Thermal conductivity of C/C composites

The thermal conductivities of the C/C composites with different matrix ratios along the *X*, *Y*, and *Z* directions are shown in Fig. 4(a–c). All samples exhibit the highest thermal conductivity along the *X* direction, whereas the values in the *Y* and *Z* directions are relatively lower. According to the Debye model[40], the thermal conductivity (λ) of C/C composites related to the phonon mean free path (*L*) can be described by the following Eq. (5):

$$\lambda = \frac{1}{3} C \cdot V \cdot L \quad (5)$$

where C represents the volumetric heat capacity and V denotes the propagation velocity of phonons. At room temperature, both C and V remain constant, and therefore the thermal conductivity of C/C composites are primarily determined by the magnitude of *L*. The thermal conduction mechanism is schematically shown in Fig. 4d, along the *X*-direction, the highly oriented continuous carbon fibers and their surrounding ordered pitch carbon layers establish a well-aligned lattice structure following graphitization, which significantly extends the *L*[41]. In contrast, the *L* is markedly shortened in the *Y* and *Z* directions due to the presence of numerous interfacial gaps and voids, as evidenced by the microstructure of the composites (Fig. 3(b–i)). As a result, the thermal conductivity of C/C composites exhibits strong anisotropy.

As the P∶G ratio decreases in the C/C composites matrices, the composites exhibit distinctly different trends in thermal conductivity along different directions. Specifically, the thermal conductivity along the *X* direction decreases. This reduction is primarily attributed to the increased graphite flake content disrupting the continuous thermal conduction pathways formed by ordered pitch carbon (Fig. 4d). Furthermore, the microstructure of the composites reveals a progressive transition from ordered to disordered alignment of the carbon fibers (Fig. 3(b–e)). Collectively, these factors shorten the *L*, ultimately reducing the thermal conductivity along this direction.

In contrast, the thermal conductivity in the *Y* and *Z* directions exhibited a continuous upward trend as

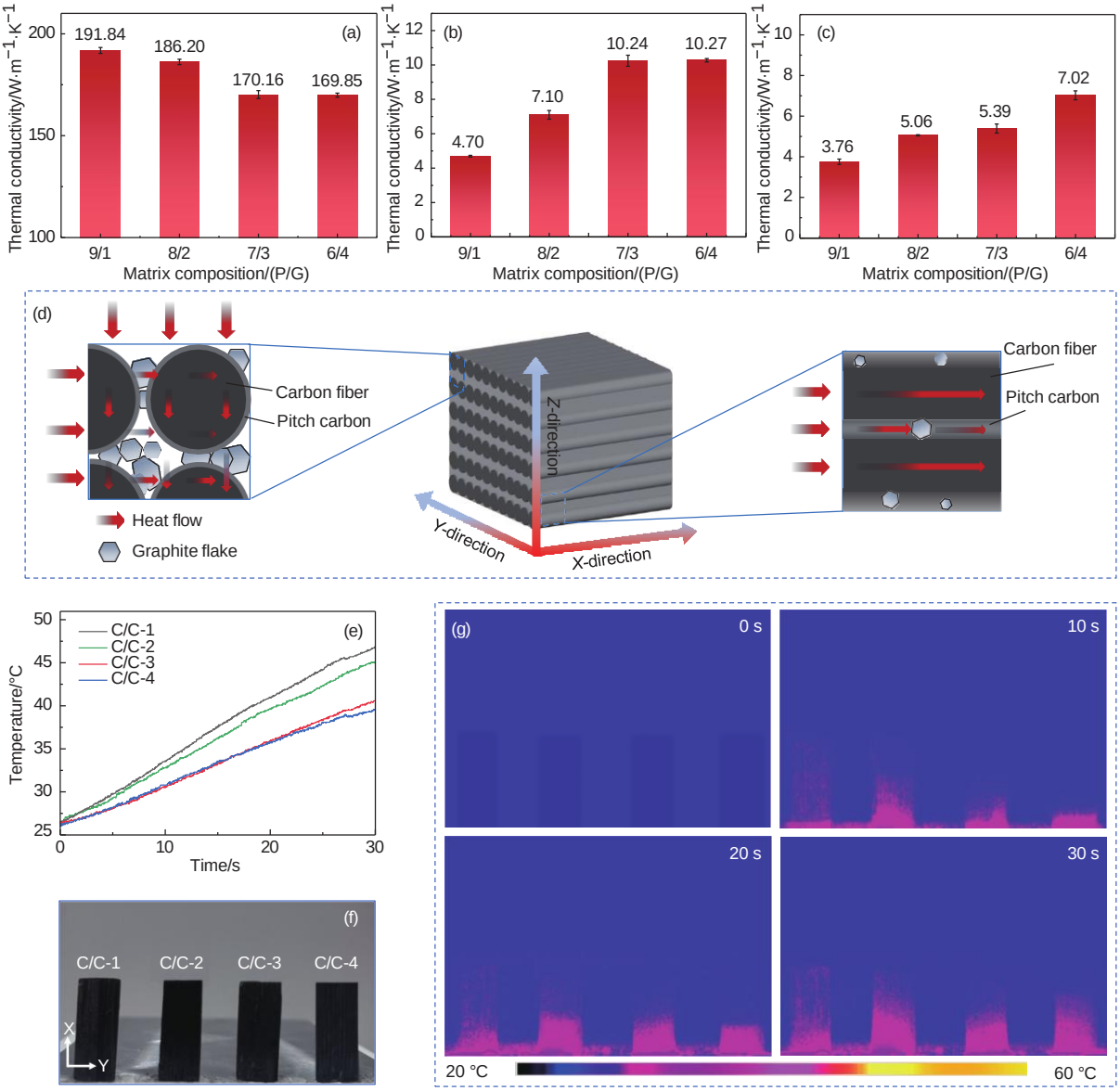

Fig. 4 (a-c) Thermal conductivity along the *X*, *Y*, and *Z* directions, respectively. (d) Thermal conduction mechanism schematic in C/C composites. (e) Top surface temperature versus heating time. (f) Sample positioning on the heater. (g) Infrared thermal images showing temperature distribution

the P∶G ratio decreased (Fig. 4(b-c)). In the heat transfer behavior of composite materials, when the filler is the primary component for thermal conduction, thermal conductivity typically increases gradually with filler content. The critical point at which the fillers begin to contact each other and form a continuous conductive network is defined as the percolation threshold[42]. This transition is characterized by a marked shift from a gradual rise to a sharp surge in thermal conductivity. In C/C composites, graphite flakes serve as highly thermally conductive fillers along the *Y* and *Z* directions, whereas the porous pitch carbon contributes minimally to thermal conductivity in these directions. Thermal conductivity in these directions increases with the flake content. When the P∶G ratio reaches 6∶4, the thermal conductivity in the *Z* direction rises sharply to 7.02 $W \cdot m^{-1} \cdot K^{-1}$, indicating that the graphite flakes have reached the percolation threshold. At this ratio, the flakes form mutual contacts that establish a continuous network, significantly extending the *L* and thereby enhancing heat transfer.

To evaluate the temperature distribution and thermal dissipation performance of the composites, strip-shaped samples with different matrix ratios were vertically placed on a heater (Fig. 4f). The surface

temperature evolution during heating was recorded using an infrared thermal camera, where red and blue regions in the thermal images represent high- and low-temperature zones, respectively. The temperature variation at the top surface of the samples over time is plotted in Fig. 4e, while the temperature distributions at 0, 10, 20 and 30 s after the onset of heating are shown in Fig. 4g. The results reveal rapid upward thermal diffusion, with rates consistent with the thermal conductivity trends of the samples, further confirming the reliability of the thermal conductivity measurements.

3.3 Electronic conductivity of C/C composites

The electronic conductivity of C/C composites with different matrix ratios along various directions is presented in Fig. 5. The conductivity is governed by the combined effects of electron migration along fibers and ordered pitch carbon layers, charge transfer between adjacent fibers, and electron hopping at defects[18]. The highest conductivity is observed in the *X* direction, where continuous carbon fibers and pitch carbon form long-range conductive pathways that facilitate efficient electron migration. However, as the P∶G ratio in the matrix decreases, the conductivity in this direction is reduced. This decline is caused by a reduction in the continuous conductive pathways provided by ordered pitch carbon, coupled with an increase in heterogeneous interfaces introduced by the graphite flakes, which collectively impede electron migration.

As shown in Fig. 5(b-c), the electronic conductivities in the *Y* and *Z* directions are significantly lower than that in the *X* direction, primarily due to the resistance encountered by electrons when traveling between fiber bundles and through porous regions in the matrix. However, both the *Y*- and *Z*-direction conductivities increase markedly as the P∶G ratio in the matrix decreases. This enhancement is attributed to 2 mechanisms: (1) the two-dimensional (2D) graphite flakes, with their high intrinsic in-plane conductivity, form conductive bridges that connect adjacent fibers, thereby facilitating inter-fiber charge transport (Fig. 3(b-i)). (2) The increased graphite flakes substantially improve the compactness in the *Z* direction (Fig. 3(f-i)), which reduces the population of voids and cracks, lowers the electrical resistance, and consequently boosts conductivity.

3.4 Mechanical properties of C/C composites

Flexural performance tests were conducted along the *X*-direction on C/C composites with different matrix ratios, with the results presented in Fig. 6a. The flexural strength initially increases and then decreases with a decreasing P∶G ratio in the matrix. The stress-strain curve of the C/C composites (Fig. 6b) exhibit a characteristic stepwise decline, indicative of pseudo-ductile fracture behavior. In C/C composites, the fracture behavior is governed by the carbon fibers, the matrix, and their interfacial interactions. An optimal interface should be strong enough to transfer stress yet sufficiently weak to enable controlled debonding and fiber pull-out, thereby improving both the strength utilization of the fibers and the overall composite strength[43]. Fracture surface analysis (Fig. 6(c–f)) reveals distinct morphological evolution across the samples. C/C-1 shows a remarkably smooth fracture surface, indicating an excessively strong interfacial bond. In this case, cracks propagate directly through the fibers[44], resulting in early failure and poor flexur-

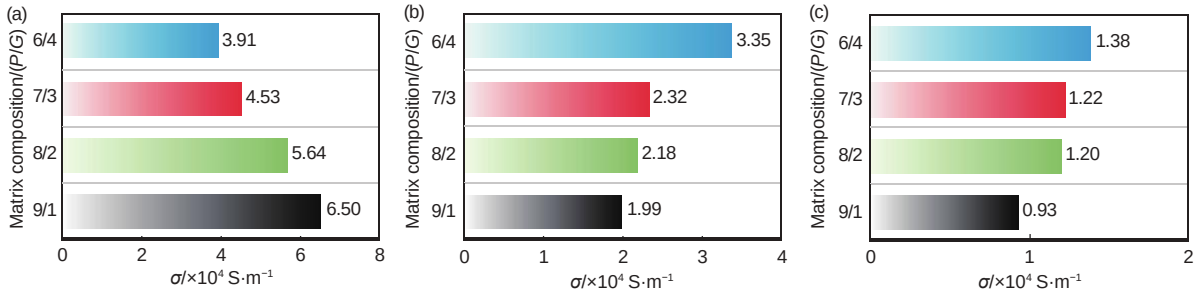

Fig. 5 Electrical conductivity of the (a) *X* direction, (b) *Y* direction and (c) *Z* direction

al performance. Although C/C-2 also exhibits a relatively clean fracture, the reduced P∶G ratio allows well-dispersed graphite flakes to deflect cracks slightly[45], leading to a marginal improvement in flexural strength.

In C/C-3, a further decrease in the P∶G ratio progressively replaces the originally strong fiber/matrix interface with weaker fiber/graphite and graphite/matrix interfaces. These interfaces are capable of enabling effective stress transfer while allowing the pull-out and delamination of fibers[46] (Fig. 6e), which contributes to the highest flexural strength of 131.84 MPa.

However, in C/C-4, the increased graphite flake content coupled with reduced pitch binder results in graphite-rich regions and poor matrix bonding. This leads to extended fiber pull-out without effective load sharing, ultimately causing a slight decline in flexural strength.

3.5 EMI shielding properties of C/C composites

As shown in Fig. 7, C/C composites demonstrate strongly anisotropic EMI shielding performance in the X-band under electromagnetic wave (EMW) incidence normal to different planes. The evaluation of EMI shielding materials relies on the concept of *SE*, which is exactly the total shielding effectiveness (SE_T). It can be determined by Eq.(6)[47], according to Schelkunoff's shielding theory.

$$SE_T = SE_R + SE_A + SE_M \quad (6)$$

where SE_R, SE_A and SE_M denote the *SE* due to reflec-

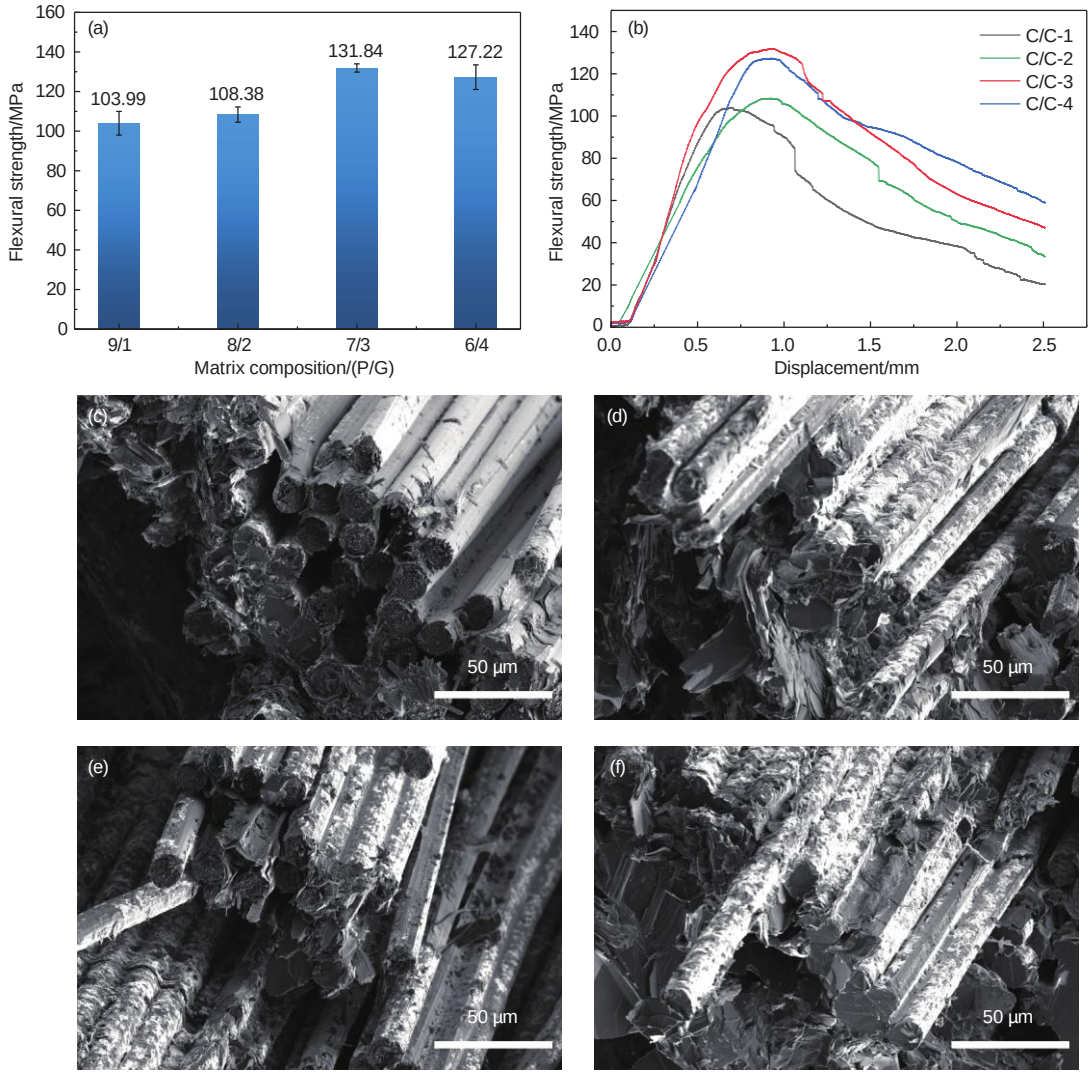

Fig. 6 (a) Flexural strength and (b) load-displacement curves of C/C composites. (c-f) Fracture morphologies of the corresponding samples: (c) C/C-1, (d) C/C-2, (e) C/C-3 and (f) C/C-4

tion, absorption, and multiple reflections, respectively. For the cases where the SE_T values greater than 15 dB[48], SE_M can be disregarded, leading to the simplified form of Eq. (7):

$$SE_T = SE_R + SE_A \quad (7)$$

SE_R and SE_A can be calculated from the reflection coefficient (R), absorption coefficient (A), and transmission coefficient (T)[49]:

$$SE^R = 10\log\left(\frac{1}{1-R}\right) \quad (8)$$

$$SE_A = 10\log\left(\frac{1-R}{T}\right) \quad (9)$$

where the coefficients R, T and A are calculated from the S-parameters, where S_{11}, S_{22}, S_{12} and S_{21} represent input reflection, output reflection, reverse transmission, and forward transmission, respectively, using the following relations[50]:

$$R = |S_{11}|^2 = |S_{22}|^2 \quad (10)$$

$$T = |S_{12}|^2 = |S_{21}|^2 \quad (11)$$

$$1 = R + T + A \quad (12)$$

A schematic of the shielding mechanism is provided in Fig. 7a. When EMW are incident on the surface, strong interaction with mobile electrons leads to significant energy loss by reflection. The residual waves that enter the material undergo repeated reflections among fiber bundles and at fiber–matrix interfaces. This multi-reflection process effectively prolongs the propagation path and enhances electromagnetic energy dissipation[51]. At the microscopic scale, EMW are subjected to continuous reflection and scattering between graphite flakes and pitch carbon, leading to progressive energy attenuation. Concurrently, charge accumulation at the heterogeneous interfaces establishes an asymmetric distribution and induces interfacial polarization relaxation, thereby dissipating electromagnetic energy as polarization loss. In paral-

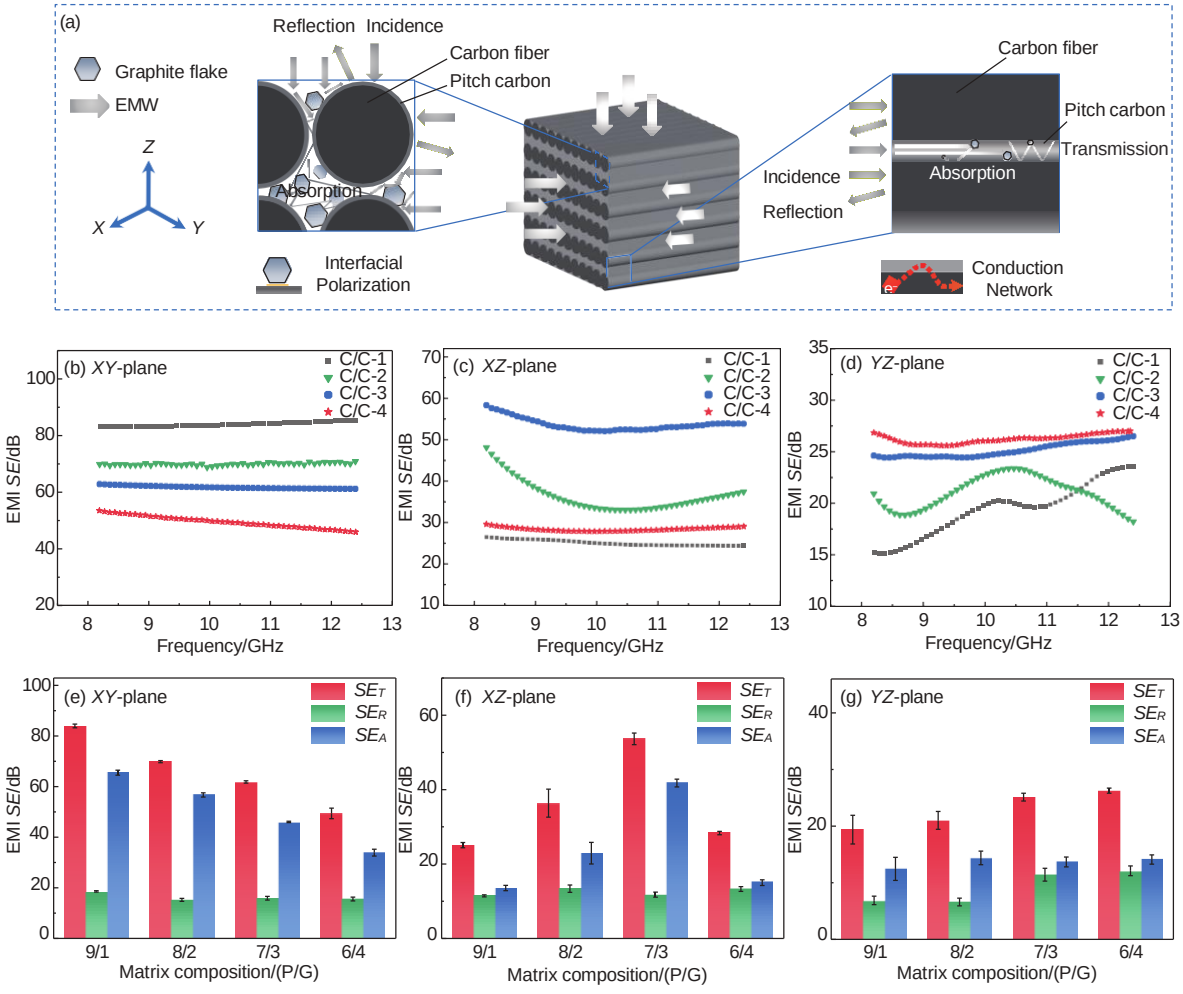

Fig. 7 (a) EMI shielding mechanism. (b-d) EMI SE and (e-g) SE_R and SE_A contributions for EMW with normal incidence on different planes

lel, the conductive network composed of carbon fibers and pitch carbon gives rise to significant conductive loss[52]. As shown in Fig. 7(e–g), the SE_A of all four samples exceeds the SE_R, indicating that the dominant EMI shielding mechanism in the composites is absorption rather than reflection. This behavior further confirms that the C/C composites fabricated by pressureless carbonization enhance the SE_T primarily through the elevation of SE_A. Furthermore, EMI *SE* exhibits multiple variations with frequency, which can be attributed to the heterogeneous distribution of electromagnetic field strength within the composites[53].

When EMW are incident on the *XY* plane (Fig. 7(b, e)), the composites achieve its highest EMI *SE*. In sample C/C-1, the maximum SE_T reaches 83.97 dB, equivalent to 99.999 999% attenuation of incident EMW, indicating near-total blocking of the electromagnetic energy. This exceptional performance originates from the porous structure resulting from the pressureless carbonization process and the high in-plane electronic conductivity ascribed to graphitization treatment[54]. The gradual decrease in SE_T with a lower P∶G ratio is primarily due to 2 factors: reduced electronic conductivity along the *X* direction and decreased porosity in the C/C composites. These changes adversely affect the SE_R and SE_A, respectively, resulting in a decrease in the SE_T.

When EMW is incident on the *XZ* plane (Fig. 7(c, f)), the SE_T initially increases and then decreases as the P∶G ratio decreases. The initial rise in SE_T is attributed to enhanced electronic conductivity along the *Y* direction. Notably, at a P∶G ratio of 7∶3, sample C/C-3 achieves the highest SE_T value of 53.66 dB, despite exhibiting a lower SE_R compared to other samples. This performance is due to a substantial increase in the SE_A, which reaches 41.83 dB. The pronounced enhancement stems from multiple reflections within the porous structure and scattering at heterogeneous interfaces, which collectively enable multi-scale EMW attenuation[55–57]. These mechanisms demonstrate the capability of the composites to convert electromagnetic energy into thermal energy. However, when the P∶G ratio further decreases from 7∶3 to 6∶4, it is accompanied by a reduction in porosity, which leads to a significant drop in the SE_A value. These results confirm that moderate porosity levels are more conducive to improving the EMI shielding performance of C/C composites.

For EMW incident on the *YZ* plane (Fig. 7(d, g)), the SE_T shows a consistent increase with decreasing P∶G ratio in the matrix. This improvement is mainly attributed to the enhanced SE_R, resulting from the combined effect of elevated electronic conductivity along the *Y* and *Z* directions and improved densification within the plane, which collectively strengthen the EMW reflection at the surface.

Table 1 compares the EMI shielding performance and density of the rapidly prepared C/C composites through pressureless carbonization with previous studies. Benefiting from the synergistic effect of its porous structure and highly conductive network, the C/C composite developed in this work achieves excellent EMI shielding performance alongside a low-density profile.

4 Conclusions

In summary, this study demonstrates a rapid fabrication route for low-density C/C composites with high EMI *SE* by pressureless carbonization. The influence of the matrix composition on the structural and properties of the composites was systematically investigated. Results indicate that although a reduced P:G ratio enhances densification, it also disrupts the ordered microstructure, resulting in distinct property changes along different material directions. All composites exhibited a bulk density below 1.10 $g \cdot cm^{-3}$. Sample C/C-1 showed exceptional directional conductive performance, with *X*-direction thermal conductivity and electronic conductivity reaching 191.84 $W \cdot m^{-1} \cdot K^{-1}$ and 6.50×10^4 $S \cdot m^{-1}$, respectively. However, both properties decreased with further reduction in the P∶G ratio. In contrast, the thermal and electronic conductivities along the *Y* and *Z* directions, although lower than those in the *X* direction, improved significantly with a decreasing P∶G ratio, attributable to continuous lateral conduction pathways formed by graphite flakes and densification effects.

Table 1 Comparison of EMI shielding performance and density among reported lightweight, high-performance structural-functional composites

Material	Frequency/GHz	EMI *SE*/dB	Density/g·cm^{-3}	Refs.
C/C-1	8.2-12.4	83.97	1.01	This work
C/C-2	8.2-12.4	69.81	1.05	This work
C/C-3	8.2-12.4	61.79	1.08	This work
C/C-4	8.2-12.4	49.34	1.09	This work
C/C	8.2-12.4	~80	1.85	[18]
SiCNW-C/C	8.2-12.4	60.50	1.70	[58]
CNT–C/C	8.2-12.4	75.20	0.93	[59]
C/SiC-Ti_3SiC_2	8.2-12.4	41.00	2.42	[60]
C_f/SiC	8.2-12.4	42.70	1.39	[61]
SiC/C–SiC	8.2-12.4	28.00	1.21	[62]
RGO/CNTs-SiCN	8.2-12.4	67.20	/	[63]
SiC nanoribbons-C/C	8.2-12.4	23.86	/	[64]
3D graphene-CNT-SiC	8.2-12.4	29.30	/	[65]

Mechanically, all composites exhibited flexural strengths exceeding 100 MPa, confirming structural robustness, with optimal graphite flake content further enhancing mechanical performance. X-band EMI shielding tests revealed that the synergy between a porous structure and high electronic conductivity resulted in outstanding EMI shielding performance, with C/C-1 achieving a *SE* of 83.97 dB under *XY*-plane EMW incidence. It was also confirmed that an appropriate porosity level further enhances the *SE*. This work provides an innovative strategy for the short-cycle fabrication of lightweight C/C composites that integrate excellent EMI shielding, high thermal conductivity and robust mechanical strength, showing great promise for applications in integrated thermal management and EMI protection.

Declaration of competing interest

All the authors declare that we have no known competing financial interests or personal relationships that could have appeared to influence the work reported in this paper.

References

[1] Chaudhary A, Kumar R, Dhakate S R, et al. Scalable development of a multi-phase thermal management system with superior EMI shielding properties[J]. Composites Part B: Engineering, 2019, 158: 206-217.

[2] Ma Z, Hao Z, Dai J, et al. Graphene-epoxy composite with dual-function of excellent microwave absorption and efficient heat dissipation[J]. Chemical Engineering Journal, 2024, 502: 157807.

[3] Wang Z, Wang S, Zhang K, et al. Heterostructured composite foam with highly efficient absorption-dominant EMI shielding capability and mechanical robustness[J]. Composites Communications, 2023, 40: 101603.

[4] Wang L, Ma Z, Zhang Y, et al. Polymer-based EMI shielding composites with 3D conductive networks: a mini-review[J]. SusMat, 2021, 1(3): 413-431.

[5] Yu H, Peng L, Chen C, et al. Regulatable orthotropic 3D hybrid continuous carbon networks for efficient bi-directional thermal conduction[J]. Nano-Micro Letters, 2024, 16(1): 198.

[6] Jia Y, Chowdhury M A R, Xu C. Electromagnetic property of polymer derived SiC–C solid solution formed at ultra-high temperature[J]. Carbon, 2020, 162: 74-85.

[7] Jia X, Shen B, Zhang L, et al. Construction of shape-memory carbon foam composites for adjustable EMI shielding under self-fixable mechanical deformation[J]. Chemical Engineering Journal, 2021, 405: 126927.

[8] Wang W, Ren C, Zheng J, et al. Ultra-high strength and flame retardant carbon aerogel composites with efficient electromagnetic interference shielding and superior thermal insulation via nano-repairing route[J]. Composites Science and Technology, 2025, 259: 110949.

[9] Wang G, Quan H, Zhang Y, et al. Development of the graphite

crystal contributing to the thermal performance of high-thermal-conductive C/C composites[J]. Ceramics International, 2024, 50(4): 6108-6119.

[10] Qing M, He Q, Wang Y, et al. Ablation resistance of C/C–Hf1-xZrxC composites under an oxyacetylene flame at above 2700 °C [J]. Composites Part B: Engineering, 2024, 287: 111855.

[11] Yin X, Han L, Liu H, et al. Recent progress in 1D nanostructures reinforced carbon/carbon composites[J]. Advanced Functional Materials, 2022, 32(35): 2204965.

[12] Li T Q, Xu Z H, Hu Z J, et al. Application of a high thermal conductivity C/C composite in a heat-redistribution thermal protection system[J]. Carbon, 2010, 48(3): 924-925.

[13] Yuan G, Li X, Dong Z, et al. Pitch-based ribbon-shaped carbon-fiber-reinforced one-dimensional carbon/carbon composites with ultrahigh thermal conductivity[J]. Carbon, 2014, 68: 413-425.

[14] Zhang X, Li X, Yuan G, et al. Large diameter pitch-based graphite fiber reinforced unidirectional carbon/carbon composites with high thermal conductivity densified by chemical vapor infiltration[J]. Carbon, 2017, 114: 59-69.

[15] Davies I J, Rawlings R D. Mechanical properties in compression of CVI-densified porous carbon/carbon composite[J]. Composites science and technology, 1999, 59(1): 97-104.

[16] Yu M, Li H, Xue K, et al. Effect of microstructure evaluation during the PIP process on macroscopic properties of C/C composites[J]. Composite Structures, 2023, 308: 116651.

[17] Zhao Y, Liu Z, Wang H, et al. Microstructure and thermal/mechanical properties of short carbon fiber-reinforced natural graphite flake composites with mesophase pitch as the binder[J]. Carbon, 2013, 53: 313-320.

[18] Xue K, Fang L, Zhang G, et al. The evaluation of microstructure of carbon/carbon composites generated by ultra-high temperature treatment towards excellent electromagnetic interference shielding property[J]. Carbon, 2022, 193: 128-139.

[19] Manocha L M. High performance carbon-carbon composites[J]. Sadhana, 2003, 28(1): 349-358.

[20] Han L, Song Q, Sun J, et al. The role of CNT in improving the mechanical strength retention rate of C/C composites during heat treatment[J]. Composites Part B: Engineering, 2020, 187: 107856.

[21] Wang H, Zheng K, Zhang X, et al. 3D network porous polymeric composites with outstanding electromagnetic interference shielding[J]. Composites Science and Technology, 2016, 125: 22-29.

[22] Zhang L Q, Yang S G, Li L, et al. Ultralight cellulose porous composites with manipulated porous structure and carbon nanotube distribution for promising electromagnetic interference shielding[J]. ACS Applied Materials & Interfaces, 2018, 10(46): 40156-40167.

[23] Zeng Z, Jin H, Chen M, et al. Lightweight and anisotropic porous MWCNT/WPU composites for ultrahigh performance electromagnetic interference shielding[J]. Advanced Functional Materials, 2016, 26(2): 303-310.

[24] Fujiura R, Kojima T, Kanno K, et al. Evaluation of naphthalene-derived mesophase pitches as a binder for carbon-carbon composites[J]. Carbon, 1993, 31(1): 97-102.

[25] Yan Q, Yang X, Zhang X, et al. Effect of graphitization temperature on microstructure, mechanical and ablative properties of C/C composites with pitch and pyrocarbon dual-matrix[J]. Ceramics International, 2023, 49(2): 2860-2870.

[26] An D, Kim K H, Lim C, et al. Effect of kneading and carbonization temperature on the structure of the carbon block for thermally conductive bulk graphites[J]. Carbon Letters, 2021, 31(6): 1357-1364.

[27] Kim M I, Cho J H, Bai B C, et al. The control of volume expansion and porosity in carbon block by carbon black (CB) addition for increasing thermal conductivity[J]. Applied Sciences, 2020, 10(17): 6068.

[28] Kim J H, Jo A Y, Choi Y J, et al. Improving the mechanical strength of carbon–carbon composites by oxidative stabilization[J]. Journal of Materials Research and Technology, 2020, 9(6): 16513-16521.

[29] Zhong B, Zhao G L, Huang X X, et al. Binding natural graphite with mesophase pitch: A promising route to future carbon blocks[J]. Materials Science and Engineering: A, 2014, 610: 250-257.

[30] Zhu J, Wang X, Guo L, et al. A graphite foam reinforced by graphite particles[J]. Carbon, 2007, 45(13): 2547-2550.

[31] Menendez R, Fernández J J, Bermejo J, et al. The role of carbon black/coal-tar pitch interactions in the early stage of carbonization[J]. Carbon, 1996, 34(7): 895-902.

[32] Blanco C, Appleyard S P, Rand B. Study of carbon fibres and carbon–carbon composites by scanning thermal microscopy[J]. Journal of microscopy, 2002, 205(1): 21-32.

[33] Rodrigues S, Marques M, Suárez-Ruiz I, et al. Microstructural investigations of natural and synthetic graphites and semi-graphites[J]. International Journal of Coal Geology, 2013, 111: 67-79.

[34] Li K, Liu Q, Cheng H, et al. Classification and carbon structural transformation from anthracite to natural coaly graphite by XRD, Raman spectroscopy, and HRTEM[J]. Spectrochimica Acta Part A: Molecular and Biomolecular Spectroscopy, 2021, 249: 119286.

[35] Zimmer J E, White J L. Disclination Structures in the Carbonaceous Mesophase[M]. Advances in liquid crystals. Elsevier, 1982.

[36] Li W Q, Zhang H B, Xiong X, et al. Influence of fiber content on the structure and properties of short carbon fiber reinforced carbon foam[J]. Materials Science and Engineering: A, 2010, 527(27-28): 7274-7278.

[37] Yuan G, Cui Z. Preparation, Characterization, and Applications of Carbonaceous Mesophase: a review[M]. IntechOpen, 2019.

[38] Xu J, Guo L, Wang H, et al. Influence of graphitization temperature on microstructure and mechanical property of C/C-SiC composites with highly textured pyrolytic carbon[J]. Journal of the European Ceramic Society, 2022, 42(5): 1893-1903.

[39] Chollon G, Siron O, Takahashi J, et al. Microstructure and mechanical properties of coal tar pitch-based 2D-C/C composites

with a filler addition[J]. Carbon，2001，39（13）：2065-2075.

[40] Yang J. Theory of Thermal Conductivity[M]. Thermal Conductivity: Theory, Properties, and Applications. Boston, MA: Springer US, 2004.

[41] Wu G P, Li D H, Yang Y, et al. Carbon layer structures and thermal conductivity of graphitized carbon fibers[J]. Journal of Materials Science，2012，47（6）：2882-2890.

[42] Shtein M, Nadiv R, Buzaglo M, et al. Thermally conductive graphene-polymer composites: size, percolation, and synergy effects[J]. Chemistry of Materials，2015，27（6）：2100-2106.

[43] Zaldivar R J, Rellick G S, Yang J M. Fiber strength utilization in carbon/carbon composites[J]. Journal of materials research，1993，8（3）：501-511.

[44] Li Y, Guo L, Song Q, et al. Simultaneous improvements in flexural strength and ductility of carbon nanotube-doped carbon/carbon composites by depositing a pyrocarbon layer on carbon fibers[J]. Ceramics International，2015，41（2）：1943-1949.

[45] Cai Y, Fan S, Liu H, et al. Mechanical properties of a 3D needled C/SiC composite with graphite filler[J]. Materials Science and Engineering: A，2010，527（3）：539-543.

[46] Li S P, L K Z, Li H J, et al. Effect of HfC on the ablative and mechanical properties of C/C composites[J]. Materials Science and Engineering: A，2009，517（1-2）：61-67.

[47] Jia H, Liang L, Liu D, et al. A review of three-dimensional graphene networks for thermal management and electromagnetic protection[J]. New Carbon Materials，2021，36（5）：851-868.

[48] Yang Y, Gupta M C, Dudley K L, et al. Novel carbon nanotube–polystyrene foam composites for electromagnetic interference shielding[J]. Nano letters，2005，5（11）：2131-2134.

[49] Zhang L, Liu M, Bi S, et al. Polydopamine decoration on 3D graphene foam and its electromagnetic interference shielding properties[J]. Journal of colloid and interface science，2017，493：327-333.

[50] Zhu S, Shi R, Qu M, et al. Simultaneously improved mechanical and electromagnetic interference shielding properties of carbon fiber fabrics/epoxy composites via interface engineering[J]. Composites Science and Technology，2021，207：108696.

[51] Yin J, Zhang J, Zhang S, et al. Flexible 3D porous graphene film decorated with nickel nanoparticles for absorption-dominated electromagnetic interference shielding[J]. Chemical Engineering Journal，2021，421：129763.

[52] Lin X, Zheng L, Wang X, et al. Developing lightweight C/ (Zr, Hf) C-SiC composite with broadband EMI shielding performance and structural stability using recycled carbon fibers[J]. Ceramics International，2025，51（20）：31456-31465.

[53] Tahalyani J, Akhtar M J, Kar K K. Graphene nanoplatelets-based lightweight flexible nanocomposites for EMI shielding application[J]. IEEE transactions on electromagnetic compatibility，2022，64（5）：1674-1682.

[54] Yang P, Li T, Li H, et al. Progress in the graphitization and applications of modified resin carbons[J]. New Carbon Materials，2023，38（1）：96-108.

[55] Li Q, Tian X, Yang W, et al. Fabrication of porous graphene-like carbon nanosheets with rich doped-nitrogen for high-performance electromagnetic microwave absorption[J]. Applied Surface Science，2020，530：147298.

[56] Yang W, Jiang B, Che S, et al. Research progress on carbon-based materials for electromagnetic wave absorption and the related mechanisms[J]. New Carbon Materials，2021，36（6）：1016-1030.

[57] Zeng Z, Zhang Y, Ma X Y D, et al. Biomass-based honeycomb-like architectures for preparation of robust carbon foams with high electromagnetic interference shielding performance[J]. Carbon，2018，140：227-236.

[58] Shen Q, Li H, Lin H, et al. Simultaneously improving the mechanical strength and electromagnetic interference shielding of carbon/carbon composites by electrophoretic deposition of SiC nanowires[J]. Journal of Materials Chemistry C，2018，6（22）：5888-5899.

[59] Liu X, Yin X, Kong L, et al. Fabrication and electromagnetic interference shielding effectiveness of carbon nanotube reinforced carbon fiber/pyrolytic carbon composites[J]. Carbon，2014，68：501-510.

[60] Fan X, Yin X, Cai Y, et al. Mechanical and electromagnetic interference shielding behavior of C/SiC composite containing Ti_3SiC_2[J]. Advanced Engineering Materials，2018，20（2）：1700590.

[61] Chen L, Yin X, Fan X, et al. Mechanical and electromagnetic shielding properties of carbon fiber reinforced silicon carbide matrix composites[J]. Carbon，2015，95：10-19.

[62] Wang H, Zhu D, Mu Y, et al. Effect of SiC/C preform densities on the mechanical and electromagnetic interference shielding properties of dual matrix SiC/C–SiC composites[J]. Ceramics International，2015，41（10）：14094-14100.

[63] Liu X, Yu Z, Ishikawa R, et al. Single-source-precursor derived RGO/CNTs-SiCN ceramic nanocomposite with ultra-high electromagnetic shielding effectiveness[J]. Acta Materialia，2017，130：83-93.

[64] Xie A, Zhang B, Ge Y, et al. The microstructure and electromagnetic interference shielding effectiveness of C/C composite surfaces modified by SiC nanoribbons@ vertically oriented graphene[J]. Journal of Materials Research and Technology，2023，25：4833-4841.

[65] Feng F, Han Z, Wei B, et al. Increasing both the electromagnetic shielding and thermal conductive properties of three-dimensional graphene-CNT-SiC hybrid materials[J]. New Carbon Materials，2024，39（6）：1178-1190.